Pd@TiO_2/carbon nanohorn electrocatalysts: reversible CO_2 hydrogenation to formic acid†

M. Melchionna,[a] M. V. Bracamonte,[a] A. Giuliani,[a] L. Nasi,[b] T. Montini,[ac] C. Tavagnacco,[a] M. Bonchio, *[d] P. Fornasiero *[ac] and M. Prato *[aef]

Accepted 4th April 2018

Direct conversion of carbon dioxide to formic acid at thermodynamic equilibrium is an advantage of enzymatic catalysis, hardly replicated by synthetic analogs, but of high priority for carbon-neutral energy schemes. The bio-mimetic potential of totally inorganic Pd@TiO_2 nanoparticles is envisioned herein in combination with Single Walled Carbon NanoHorns (SWCNHs). The high surface nano-carbon entanglement templates a wide distribution of "hard-soft" bimetallic sites where the small Pd nanoparticles (1.5 nm) are shielded within the TiO_2 phase (Pd@TiO_2), while being electrically wired to the electrode by the nanocarbon support. This hybrid electrocatalyst activates CO_2 reduction to formic acid at near zero overpotential in the aqueous phase (onset potential at $E < -0.05$ V *vs.* RHE, pH = 7.4), while being able to evolve hydrogen *via* sequential formic acid dehydrogenation. The net result hints at a unique CO_2 "circular catalysis" where formic acid *versus* H_2 selectivity is addressable by flow-reactor technology.

Broader context

Sustainability is a central theme of today's scientific community. In conjunction with the growth of the world population and the fast depletion of fossil fuels, there is a need to define new concepts that diversify the supply of energy and make it sustainable. One intriguing solution is the environmentally benign (photo- or electro-assisted) reutilization of anthropological CO_2: the strategy is to convert it back to carbon fuels, creating a carbon-neutral cyclic scheme. On the other hand, an alternative concept is the utilization of green energy vectors, such as hydrogen. However, the reduction of CO_2 and H_2 evolution are both challenging processes, requiring complex engineering of catalysts in order to trigger the reactions with low activation energy and high selectivity. Inspired by the natural formate dehydrogenase (FDH) enzymes, herein, we describe a nanostructured ternary electro-catalyst that is able to fulfil a double action: it can reduce CO_2 to formic acid with low overpotential and high current efficiency, and it can evolve hydrogen *via* sequential formic acid dehydrogenation. Mechanistic insights reveal that the nanocatalyst mimics the enzyme multi-functional behavior and the neat result is the use of CO_2 as a reversible energy vector.

Introduction

The electrocatalytic hydrogenation of CO_2 to formic acid (HCO_2H) and/or to its conjugate base, formate (HCO_2^-), is of central importance for carbon-neutral energy schemes, where CO_2 is used as a reversible storage/release vector for H_2-based technologies.[1] CO_2 reduction is used in nature as a key strategy to store energy in chemical bonds. However, its artificial replica under abiotic conditions is highly inefficient due to severe thermodynamic and kinetic hurdles related to CO_2 capture and activation.[2]

A new paradigm has been recently introduced by the direct use of purified formate dehydrogenase (FDH) enzymes as electrocatalysts, which provides a definite landmark for CO_2/formate interconversion with fast rates in water at neutral pH.[2–4] FDH-based electrocatalysis is conceptually unique *vis-à-vis* the near-equilibrium working potential and its product specificity.[3–5] However, this approach is plagued by protein purification and stability issues, together with formidable scaling-up problems, which hamper any viable exploitation. Therefore, the invention of synthetic catalysts and functional electrodes mimicking the enzymatic performance with robust chemical architectures remains

[a] Department of Chemical and Pharmaceutical Sciences, INSTM, University of Trieste, Via L. Giorgieri 1, 34127 Trieste, Italy. E-mail: pfornasiero@units.it, prato@units.it
[b] CNR-IMEM Institute, Parco area delle Scienze 37/A, 43124 Parma, Italy
[c] ICCOM-CNR, University of Trieste, Via L. Giorgieri 1, 34127 Trieste, Italy
[d] ITM-CNR and Department of Chemical Sciences, University of Padova, Via F. Marzolo 1, 35131 Padova, Italy. E-mail: marcella.bonchio@unipd.it
[e] Carbon Nanobiotechnology Laboratory, CIC biomaGUNE, Paseo de Miramón 182, 20009 Donostia-San Sebastian, Spain
[f] Basque Fdn Sci, Ikerbasque, Bilbao 48013, Spain

a priority for selective CO_2 processing.[1,3] To date, while several bio-inspired molecular catalysts and nano-materials have been successfully developed for the electrocatalytic reduction of CO_2 to CO, two-electron hydrogenation to formate is still achieved with a too high overpotential, poor selectivity and limited appeal.[2] Recent case-studies highlight that a functional synergy of the active metal-site with its proximal environment provides a key strategy for: (i) capturing CO_2 with favorable absorption/activation equilibria; (ii) low-energy proton coupled electron transfer mechanisms (PCET); (iii) the stabilization of selective hydride intermediates enabling the direct hydrogenation of CO_2.[3] In this notion, an "ideal" catalyst should be effective for both the direct CO_2-to-HCO_2H conversion, and the back-dehydrogenation reaction, which eventually liberates H_2 and CO_2 from HCO_2H decomposition. According to this scheme, CO_2/HCO_2H interconversion through reversible and/or sequential catalytic steps is of central importance as it expands the scope of formic acid synthesis, from a pure commodity "niche" chemical (*ca.* 800k ton per year) to a liquid source of H_2 storage (4.3 wt%) with a carbon-neutral net balance.[6–8]

Continuous H_2 production is currently pursued through direct proton/water electrocatalytic reduction. However and despite some recent encouraging systems using earth-abundant, non-noble metal electrocatalysts, such as cobalt,[9,10] molybdenum,[11,12] and iron,[13] costly Pt-based cathodes are still the preferred choice on account of their low overpotential, wide pH range applicability and high turnover performance.[14–16] Therefore, the alternative $CO_2 \rightarrow HCO_2H \rightarrow H_2 + CO_2$ cycle, where CO_2 mediates water reduction/hydride transfer mechanisms at the gas–liquid interface, provides an appealing electrocatalytic route for a CO_2-circular hydrogen economy.

Modified electrodes able to favourably and selectively reduce CO_2 based on the use of noble metals have been massively investigated, with platinum being surely the most employed metal even in recent reports.[17–19] Pd is a possible intriguing alternative due to its lower cost as compared to Pt or Au, as well as its recently reported low toxicity,[20] which alleviates scaling-up issues. Pd-containing electrocatalysts have been successfully tuned to target CO_2 electro-hydrogenation in combination with carbon-rich supports,[21] conductive polymers[22] or Pt-heterojunctions.[23] In particular, we have recently shown that Pd nanoparticles (Pd-NPs) on single wall carbon nanotubes trigger direct electro-catalytic water reduction at neutral pH and with low applied potentials (50 mV).[24] Pd-based nanocatalysts have also been recently shown to facilitate the dehydrogenation of formic acid at ambient temperatures.[25] Following these concepts, we report herein the integration of Pd nanoparticles (Pd-NPs) on oxidized Single Walled Carbon NanoHorns (ox-SWCNHs) and their stabilization using a TiO_2 outer-shell, by taking inspiration from previous studies by some of us on Pd nanoparticles embedded into oxide matrices and hierarchical catalysts.[26–29] The resulting Pd@TiO_2/ox-SWCNHs heterostructures feature an unprecedented triple-junction electrocatalytic interface that is effective for a cascade transformation involving CO_2-to-HCO_2H reduction and HCO_2H-to-H_2 decomposition, thus using CO_2 as an organo-catalytic mediator (Scheme 1). The resulting electrocatalyst enables selective CO_2 reduction at a mild potential

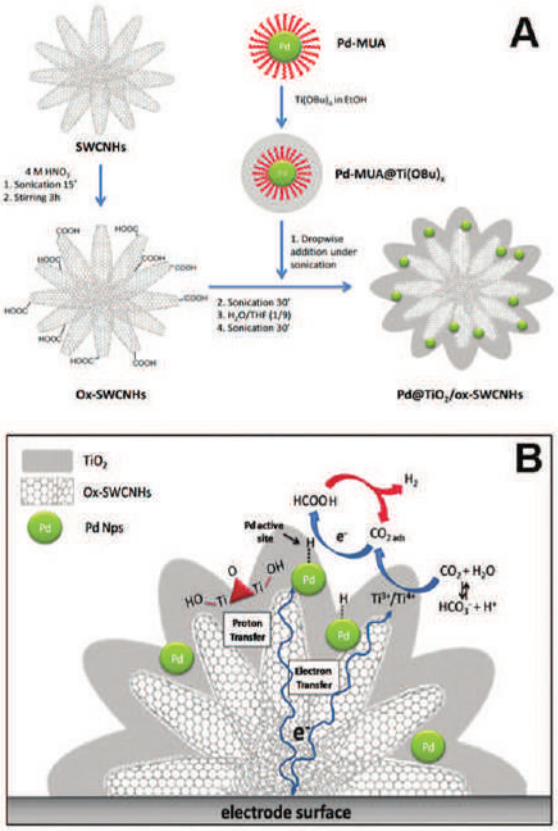

Scheme 1 (A) Schematic synthesis of Pd@TiO_2/ox-SWCNH hetero-structures by the sol–gel inclusion of capped Pd-NPs (MUA = mercapto-undecanoic acid) within a TiO_2 shell, upon controlled hydrolysis in the presence of oxidized SWCNHs, and (B) scheme of the electrocatalytic hydrogenation mechanism envisaged for the conversion of CO_2 to formic acid (blue arrows) and its decomposition (red arrows) at the Pd@TiO_2/ox-SWCNH triple functional interface (−0.2 V *vs.* RHE). For convenience, we presented a 2D section of the electrocatalytic material.

(∼−0.2 V *vs.* RHE) as the dominant pathway, overriding the competitive reduction of water to hydrogen (HER mechanism, at ∼−0.4 V *vs.* RHE). It is noteworthy that H_2 evolution is observed over time, as a product of the catalytic decomposition of formic acid accumulating in the system. Indeed, under CO_2-free conditions, no H_2 is observed, underpinning the key role of CO_2 as an intermediate. Our results point to the electrocatalytic formation of "Pd–H" intermediates at the crossroad of concurrent hydrogenation/de-hydrogenation pathways, involving the CO_2/HCO_2H couple. The final outcome is a continuous H_2 evolution at a lower overpotential (200 mV gain), in the presence of a steady-state formic acid concentration, implying a circular CO_2 consumption/release process. Taking advantage of the exceptionally high faradaic efficiency of the HCO_2H production (up to ∼95% in the initial 5 minutes then reaching a 40% yield after 1 h), kinetic control of the reaction profile under a flow regime is envisaged herein as a tool to switch the product selectivity favouring the commodity chemical. Indeed, when the HCO_2H product is extracted from the electrolysis phase at selected chronoamperometry – time intervals, H_2 evolution is stopped while the formate selectivity is restored and this behaviour is confirmed in multiple on/off experiments.

Results and discussion

Synthesis and characterization of the electrocatalytic Pd@TiO_2/ox-SWCNH heterostructures

The synthetic design of the organic–inorganic nano-material has been planned with the twofold aim of: (i) exploiting the high surface area and morphology of the nanohorn scaffold (SWCNH) as the template; (ii) providing "soft" Pd sites within a "hard" TiO_2 metal-oxide environment. The latter aspect is instrumental to control CO_2/H_2O binding equilibria at bimetallic sites,[30] while favoring Pd-hydride phases, and shielding the ultra-small Pd-NPs against irreversible agglomeration and poisoning (Scheme 1).[31,32] Moreover, the SWCNH connectivity guarantees the electrical wiring of the Pd-active sites, as a result of their unique conical geometry with protruding nano-tips that work as terminal "electron collectors" and boost the charge mobility.[33,34] Such behavior is further implemented by the strong tendency of the SWCNHs to aggregate into flower-like superstructures, with an increased surface area and improved gas adsorption behavior.[35] Gas absorption is expected to modulate the SWCNH conductivity properties.[36]

The Pd@TiO_2 precursors are readily obtained by following a literature protocol[37] and used for the sol–gel integration of the oxidized SWCNHs (ox-SWCNHs). The controlled oxidation of the SWCNHs yields an optimal surface distribution of carboxylate (COOH) and/or epoxy-alcoholic functions (C–O–C, C–OH) needed to anchor the sol–gel blend. The oxidation treatment is also instrumental to the opening of reactive nano-windows (*i.e.* opening of the SWCNH tips and defects in the polyaromatic framework),[38] that further enhance the material surface area (ox-SWCNHs, BET $\sim$ 1400 $m^2\ g^{-1}$) and its interaction with the sol–gel matrix.[39]

Thermogravimetric analysis (N_2-TGA) has been used to assess the degree of SWCNH oxidative functionalization, which accounts for 11% by weight (Fig. S1, ESI†). The target nano-hybrid Pd@TiO_2/ox-SWCNHs is finally obtained after the controlled hydrolysis of the Ti alkoxide precursors in a H_2O/THF solvent mixture. As a term of comparison, the Pd-free analogue, TiO_2/ox-SWCNHs, is obtained by a similar sol–gel strategy. The O_2-TGA analysis of both hybrid materials indicates that the carbon phase accounts for about 75 wt%, with the remaining 25 wt% being ascribed to the metal-oxide components, in agreement with the synthetic protocol conditions. Analogously, the approximate overall content of Pd is calculated to be about 1.5 wt%. Such a value is further confirmed by the ICP-AES analysis of the material, which provides an exact loading of 1.45%. The intimate carbon/metal/metal oxide contact of the hybrid material is responsible for the anticipation (by about 50 °C) of the onset of combustion temperature as compared to the SWCNH scaffold alone. This effect is caused by the presence of the Pd nanoparticles which can catalyze the combustion of the carbon scaffold.

Direct evidence of the material morphology is obtained by High Resolution Transmission Electron Microscopy (HRTEM), in combination with High-Angle Annular Dark-Field imaging (HAADF) and Energy-Dispersive X-ray Spectroscopy (EDX) element mapping, collected for the resulting materials at three stages of fabrication complexity, namely: ox-SWCNHs, TiO_2/ox-SWCNHs and Pd@TiO_2/ox-SWCNHs (Fig. 1). The inspection of the microscopy images confirms: (i) the supramolecular architecture of the SWCNH secondary aggregates with diameter in the range of 50–80 nm (ox-SWCNHs Fig. 1A); (ii) the adhesion of a thin shell of TiO_2 decorating the SWCNH particles at their outer rim and protruding edges (TiO_2/ox-SWCNHs Fig. 1B); (iii) the embedding of the ultra-small Pd-NPs with an average diameter of 1.5 nm and a standard deviation of 0.36 nm (Fig. 2), co-localized with the metal-oxide phase, displaying a broad coverage all over the interdigitated SWCNH phase (Pd@TiO_2/ox-SWCNHs Fig. 1C). Homogeneous dispersion of the Pd NPs is well visible in the HAADF-STEM image as bright spots, from where the particle size distribution was calculated (Fig. 2A and Fig. S14, ESI†). Notably, HAADF-STEM inspection of the material after catalysis shows no change in the structure, with the Pd NPs not undergoing any aggregation (Fig. S15, ESI†).

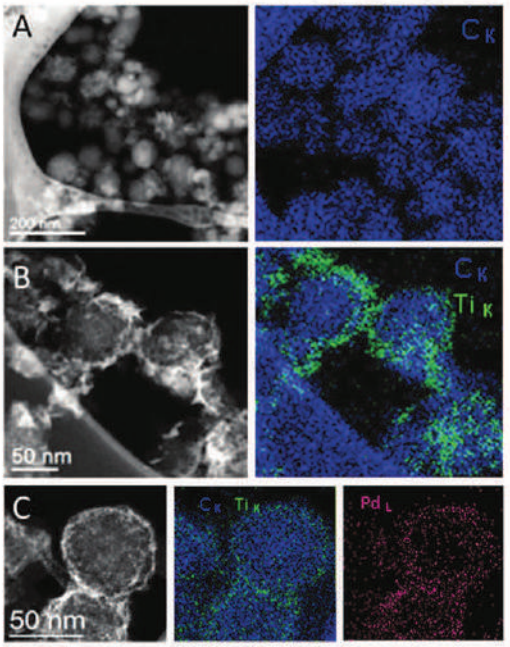

Fig. 1 Representative HAADF (black and white) and corresponding EDX maps (colours) of the SWCNH-based hetero-structures: (A) ox-SWCNHs, (B) TiO_2/ox-SWCNHs, (C) Pd@TiO_2/ox-SWCNHs.

In accordance with the very low thermal treatment of the present materials, Fast Fourier Transform (FFT) and selected area electron diffraction (SAED) analyses did not reveal any crystalline area for TiO_2, which turns out to be amorphous. This may be one of the parameters defining the electrocatalytic properties of the material. Namely, the onset potential for the competing water electrolysis in our case is significantly more negative than that found for the CNT-based analogue material, where the titania layer was crystallized through thermal annealing.[24] This imparts a wider potential window between the CO_2 reduction and proton reduction processes, contributing to enhanced selectivity and driving the mechanism of HER.

Raman spectra collected for ox-SWCNHs show the typical D and G band pattern for these nanostructures: the defect-induced

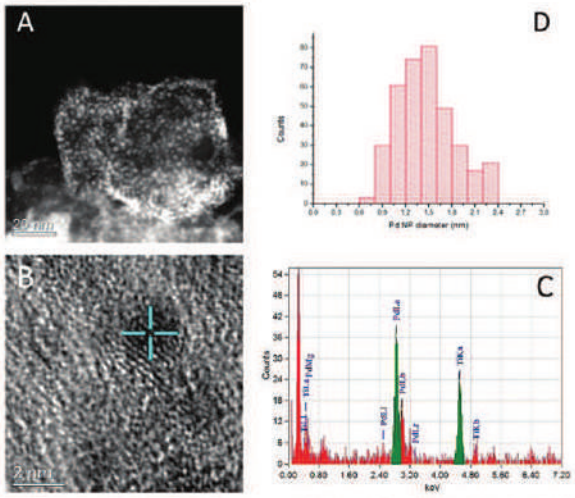

Fig. 2 Representative STEM images of the catalyst Pd@TiO_2/ox-SWCNHs (A), HRTEM image showing the size of the Pd nanoparticles (B), EDX spectrum (C) and Pd particle size distribution calculated from the STEM images.

D band at ~1330 cm^{-1}, the graphitic G band at ~1580 cm^{-1} and the D second order harmonic 2D band at ~2665 cm^{-1} (Fig. S2A, ESI,† black trace). The ratio between the intensities of the D and G bands (I_D/I_G ratio) is a semiquantitative indication of the degree of covalent modification of the conjugate framework. For the oxidized ox-SWCNHs, the I_D/I_G ratio (~1.27) is not significantly affected with respect to the pristine material, as a result of mild oxidation conditions, thus indicating a minimal perturbation of the SWCNH properties by surface defects.[40] In agreement with the SAED analysis, no peaks associated with crystalline TiO_2 modes are observed in the Raman spectra of the TiO_2/ox-SWCNHs or Pd@TiO_2/ox-SWCNHs (Fig. S2A, ESI,† red and green traces) due to their amorphous phase. Consistently, irradiation with higher Raman laser powers (>5 mW) induces local crystallization, proved by the appearance of five Raman peaks characteristic of the TiO_2 anatase phase at 146 cm^{-1}, 198 cm^{-1}, 395 cm^{-1}, 513 cm^{-1} and 639 cm^{-1} [41] (Fig. S2B and S3, ESI†). FT-IR analysis has been used to address the surface functional groups of the final nano-hybrid Pd@TiO_2/ox-SWCNHs (Fig. S4, ESI†), whereby signature peaks observed at ~800, 1100, 1400, 1600, and 3400 cm^{-1}, are respectively ascribed to the vibration modes of the metal-oxide O–Ti–O groups,[24] and those of the C–O, C═C and C═O moieties of the carbon phase, while the broad O–H absorption band likely includes the contribution of the C–O–H, (CO)O–H and Ti–O–H functions.[42] Therefore, the FT-IR evidence points to the presence of a hydrated coordination sphere, settled on the metal-oxide phase, which mitigates the hydrophobicity of the nano-carbon scaffolds, while promoting the proton/hydride transfer reaction at the Pd-active sites under reducing conditions (Scheme 1).

The accessibility of the Pd-NPs has been probed by CO chemisorption experiments on the Pd@TiO_2/ox-SWCNHs, performed at 35 °C, which confirm the TiO_2 porous structure (Fig. S5, ESI†), yielding a Pd surface area of about 1.47 m^2 g^{-1} (Fig. S6, ESI†). This value is consistent with the size and the amount of Pd-NPs present in the sample. Furthermore, the specific surface area (BET) of the Pd@TiO_2/ox-SWCNH hybrid remains significant (BET ~ 148 m^2 g^{-1}), as shown by N_2 physisorption analysis (Fig. S7, ESI†). Hence, the porosity of the TiO_2 matrix allows accessibility of the embedded Pd nanoparticles.

Electrochemical characterization and bulk electrocatalysis experiments

The electrocatalytic activity of the hierarchical nano-hybrids was initially evaluated by Cyclic Voltammetry (CV) experiments, performed in phosphate buffer (pH = 7.4), at a scan rate of 30 mV s^{-1} under both N_2- and CO_2-saturated solutions (Fig. 3). The control survey obtained under N_2 saturation, for the material precursors and for the final nano-hybrid confirms the inertness of the ox-SWCNHs within the explored potential window (black line in Fig. S8, ESI†), while the redox signatures recorded at −0.65 V and −0.35 V *vs.* RHE for the TiO_2/ox-SWCNHs can be readily ascribed to the Ti^{4+}/Ti^{3+} sites of the metal-oxide shell.[43] It is noteworthy that the CV curve recorded for the Pd@TiO_2/ox-SWCNHs appears to be dominated by the Pd-NPs (green line in Fig. S8, ESI†). These are responsible for two cathodic peaks centered at 0.40 V and −0.25 V *vs.* RHE ascribed to the reversible reduction of PdO formed during the oxidative potential scan at E > 0.65 V *vs.* RHE.[44,45] It is noteworthy that, in accordance with previous studies,[24] the electrocatalytic HER arising from the reduction of water is visible in the CV scan under N_2 as a cathodic wave at an onset potential of about −0.4 V *vs.* RHE. The calculation of the electroactive surface area (EASA) of the Pd@TiO_2/ox-SWCNH modified electrodes is readily accomplished by considering the requirement of a charge value of 405 μC cm^{-2} for the reduction of the PdO monolayer, which yields an EASA value of (0.22 ± 0.04) cm^2 which corresponds to ~17 m^2 g^{-1} after normalization by the grams of catalyst. For the sake of comparison, we prepared a TiO_2-free reference, Pd/ox-SWCNHs, with a nominal Pd title of 1.5%, *via* the $NaBH_4$ reduction of the K_2PdCl_4 precursor, after adsorption onto the ox-SWCNHs. TEM analysis confirms the presence of the Pd-NPs on the nanocarbon

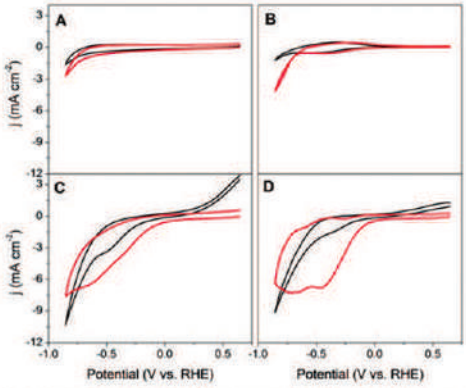

Fig. 3 CVs at GCEs modified with the ox-SWCNHs (A), TiO_2/ox-SWCNHs (B), Pd/ox-SWCNHs (C) and Pd@TiO_2/ox-SWCNHs (D) in N_2 (—) and CO_2 (—) saturated 0.1 M phosphate buffer solution, pH 7.4. Scan rate: 0.05 V s^{-1}.

scaffold (Fig. S9, ESI†), while the resulting electrode displays a calculated EASA of (0.15 ± 0.02) cm^2, thus providing a key control material. It must be noted that the TiO_2-free material has a broader particle size dispersion (Fig. S9, ESI†) with averagely larger Pd nanoparticles. Nevertheless, a reliable estimate of the effect of TiO_2 can be gathered from the observed onset potentials, being associated with the mechanism of catalysis. Moreover, the Pd/ox-SWCNHs serve as the reference to evaluate the stability of the catalyst (see later). The CV scans highlight the different response of the ox-SWCNH (A), TiO_2/ox-SWCNH (B), Pd/ox-SWCNH (C) and Pd@TiO_2/ox-SWCNH (D) modified GC electrodes when exposed to a CO_2-saturated solution (pH to 6.5) as compared to N_2 saturation conditions (red *vs.* black lines, Fig. 3). While the modest current variation observed for the ox-SWCNHs is likely ascribed to a conductivity change of the nano-carbon scaffold under the CO_2 saturated conditions (red line, Fig. 3A), the redox shift and catalytic current observed for the TiO_2/ox-SWCNHs indicates the occurrence of coordination equilibria and CO_2 electrocatalytic reduction at >-0.65 V *vs.* RHE (red line, Fig. 3B). When the Pd-NPs are integrated into the nano-catalyst formulation, yielding either Pd/ox-SWCNHs or Pd@TiO_2/ox-SWCNHs, a remarkable enhancement of the electrodic response is noted for both catalysts under CO_2 (red line, Fig. 3C and D). However, a strikingly different behaviour is observed for the final Pd@TiO_2/ox-SWCNH nanohybrid, in comparison with all the other combinations (cfr Fig. 3A–C with Fig. 3D). The catalytic increase of the cathodic current produces two well-defined peaks observed respectively at $E_1 = -0.45$ V and $E_2 = -0.69$ V *vs.* RHE. A steep current increase already occurs at $E < -0.05$ V, leading to a four-fold enhancement of the faradaic density current at -0.45 V, when compared to the TiO_2/ox-SWCNHs/GCE response, and to a clear shift of the reduction onset (*ca.* 55 mV), with respect to the Pd/ox-SWCNHs.

These observations point to a synergy of the ternary Pd@TiO_2/ox-SWCNH hybrid catalyst in the electrocatalytic reduction of CO_2 at a low overpotential regime, showing that all three components are necessary to access a superior catalytic behavior (Fig. 3D). The selectivity of the electrocatalytic reduction by the Pd@TiO_2/ox-SWCNHs has been addressed under bulk-electrolysis conditions at a constant applied potential (-0.2 V *vs.* RHE), using a standard three-electrode cell, integrating an Ag/AgCl (3 M KCl) reference electrode and a Pt counter electrode, with a Pd@TiO_2/ox-SWCNH modified Toray carbon working electrode.

The Faradaic efficiency of the product (% FE, see equations in the Experimental section) was determined by quantitative analysis of the electrolyte solution and head space, performed by Ionic Liquid and Gas Chromatography (ILC, GC). At an applied potential as low as -0.2 V *vs.* RHE (0.1 M phosphate buffer (pH = 7.4)), formic acid selectivity peaks within the first 5 minute of electrolysis, yielding a maximum of 75% FE, while H_2 accounts for the remaining 25%. At longer run times, H_2 evolution dominates with >95% FE after 1 hour of electrolysis. Isotope labelling experiments (using $^{13}CO_2$) confirm that formic acid accumulating during electrolysis (*ca.* 1.6×10^{-6} mol, mass activity: 9 mA mg_{Pd}^{-1}) is produced from CO_2 as detected by mass spectrometry (Fig. S10, ESI†) and NMR (Fig. S11, ESI†). To address the origin of H_2 evolution, control experiments were performed under an inert Ar atmosphere (Fig. 4, black line) showing that: (i) in the absence of CO_2, the current density remains low ($j_{tot} \sim -0.50$ mA cm^{-2}) with no H_2 evolution; (ii) formic acid addition (0.23 M) produces a sharp recovery of a negative current density with the simultaneous production of CO_2 and H_2 (Fig. 5a); (iii) a similar behaviour is also observed in the absence of PBS buffer, when $NaClO_4$ is used as the supporting electrolyte (pH after CO_2 saturation <4, see Fig. 4, red line).

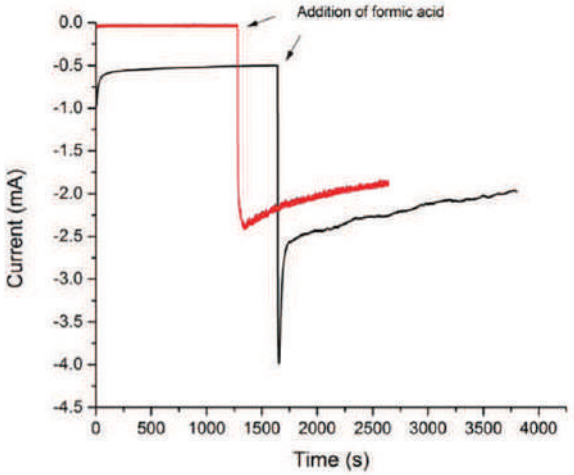

Fig. 4 Chronoamperometry of the GC electrode modified with the Pd@TiO_2/ox-SWCNHs at -0.2 V (*vs.* RHE) in PBS at pH 6.5 under an Ar flow with the addition of formic acid (black line) and chronoamperometry of the Pd@TiO_2/ox-SWCNHs at -0.13 V (*vs.* RHE) in $NaClO_4$ at pH 3.6 under an Ar flow with the addition of formic acid (red line). Quantity of formic acid added: 70 μL, final concentration of formic acid 0.23 M.

These observations point to a step-wise mechanism where HCO_2H is initially formed from CO_2 and then decomposed by the Pd@TiO_2/ox-SWCNHs, thus reaching a steady state concentration under an electrocatalytic regime. Pd nanoparticles have been reported to decompose formic acid at neutral pH and in the presence of basic sites.[46] In the present case, H_2 evolution is ascribed to the decomposition of the electrocatalytically generated HCO_2H, thus implying a mechanism based on CO_2 cycling, promoted at the Pd@TiO_2/ox-SWCNHs and favoured with respect to direct water reduction. In order to reduce HCO_2H decomposition, bulk electrolysis was performed in an unbuffered solution (pH = 3.6, CO_2 atmosphere, 0.5 M $NaClO_4$) at -0.13 V (*vs.* RHE). Under these conditions, HCO_2H is produced in quantitative yield (FE > 99%) in the first 5 minutes of electrolysis, and it levels off to 40% FE after 1 h, upon H_2 evolution (60% FE) observed as a product of formic acid decomposition (Fig. 5). The rates of formation of HCOOH and H_2 show that there is an induction time in the production of H_2 due to the initial build-up of formic acid in solution (Fig. 5).

Long-term performance and electrocatalyst stability

Under bulk electrolysis conditions (-0.20 V, 0.10 M phosphate buffer, pH 7.4) the total geometric current density (j_{tot}) settles

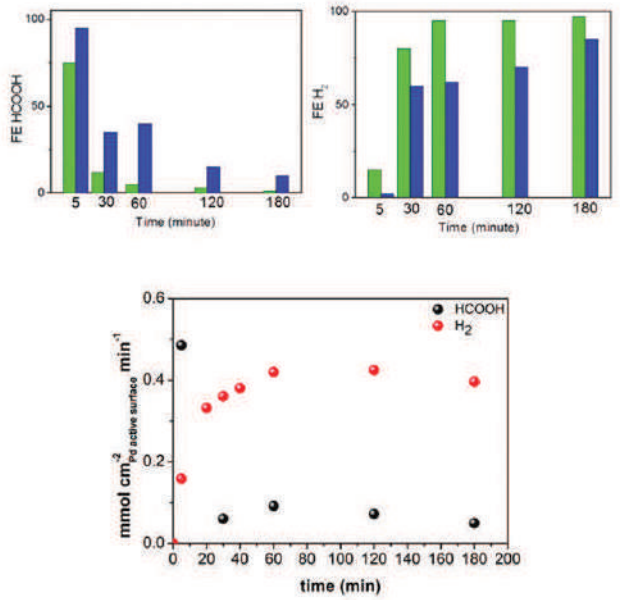

Fig. 5 Top: Faradaic efficiency in formic acid (left) and in hydrogen (right) over time at different times of the chronoamperometric experiments in PBS (green bars) and $NaClO_4$ (blue bars); bottom: rates of formation of H_2 and HCOOH by the Pd@TiO_2/ox-SWCNHs in $NaClO_4$ electrolyte over three hour long electrocatalytic experiments.

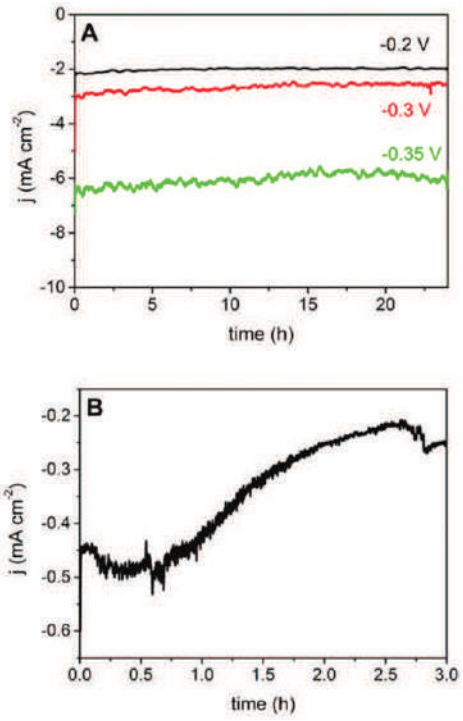

Fig. 6 Current–time profile of the Pd@TiO_2/ox-SWCNHs maintained at −0.2 V (black line), −0.30 V (red line) and −0.35 V (green line) (*vs.* RHE). Supporting electrolyte: 0.10 M phosphate buffer solution, pH 7.4. The Toray carbon electrode was modified by drop casting using 200 μL of 3.0 mg mL^{-1} (A) Pd@TiO_2/ox-SWCNHs and (B) Pd/ox-SWCNHs. The fixed potential in (B) is −0.20 V.

at a value of ~−2.00 mA cm^{-2} and maintains a very stable profile, with a negligible, <5%, decrease over 48 h of electrolysis (Fig. S12, ESI†). The stability of the Pd@TiO_2/ox-SWCNHs turned out to be excellent even at higher potentials (−0.30 V and −0.35 V, Fig. 6A), although increasing the overpotential resulted in a decrease in the FE in formic acid. The improved stability supplied by the titania layer was confirmed by comparing the catalytic stability of the Pd@TiO_2/ox-SWCNHs with that of the Pd/ox-SWCNHs under the same catalytic conditions. In contrast to the Pd@TiO_2/ox-SWCNHs, the TiO_2-free catalyst undergoes a fast deactivation at −0.2 V, with a decrease in the current density of about 50% already after 3 hours (Fig. 6B). This fact was already observed in a previous study by Kanan *et al.* and ascribed to the aggregation of the Pd NPs over electrolysis time with a consequent decrease in the EASA.[21]

Indeed, the TEM analysis of the recovered Pd/ox-SWCNH catalyst shows a significant NP aggregation after 3 hours of electrolysis, and particle leaching (Fig. S13, ESI†). Hence, the remarkable current stability proves the effectiveness of the TiO_2 phase in preventing the agglomeration and leaching of the Pd-NPs. In addition to Pd sintering, the drop in current was also related by Kanan to a poisoning of the Pd NPs over time due to concomitant formation of CO, which can coordinate to the metal and inhibit the active sites. In the present case, the selectivity of the CO_2 reduction step was extremely high, with no CO detected through continuous gas chromatography sampling of the cell head-space at 20 minute intervals, which also ruled out the presence of any other carbon-derived gases such as methane and ethylene. A control experiment was performed by adding CO (0.5%) to the gas mixture, confirming the poisoning effect on the Pd@TiO_2/ox-SWCNHs, with a current loss of *ca.* 20%.

The electrocatalyst selectivity and current performance is maintained upon recycling of the functional electrode in a sequence of three chronoamperometric experiments, switched off after one hour of electrolysis (see Fig. S16, ESI†). In these experiments, the electrolyte solution, where formic acid accumulates, is replaced at an early stage of the process, so as to guarantee a continuous peak formation of HCO_2H by the Pd@TiO_2/ox-SWCNH electrocatalyst, slowing down its decomposition. This strategy can be efficiently implemented under a flow-regime, by taking advantage of the high FE (>99%) achieved for HCO_2H at a low contact time.

Notably, the catalyst intrinsic activity is achieved with low Pd loadings (nominal Pd loading 1.5 wt%), which highlights the unique role of the hierarchical nano-interfaces to boost CO_2 activation. The turnover frequency (TOF) for the optimized H_2 evolution can be calculated from chronoamperometric experiments (see calculation details in the ESI†) and turns out to be ~26 500 h^{-1} at −0.2 V in PBS, by far exceeding the performance of the state-of-the-art formic acid dehydrogenation catalysts, namely Pd-NPs on carbon nanospheres (~7300 h^{-1}).[47]

In analogy with the recent work by Kanan and coworkers, the electrocatalytic mechanism probably involves the generation of Pd–H active sites responsible for the selective CO_2 reduction to formic acid (Scheme 1).[21] This proposal is supported by Tafel

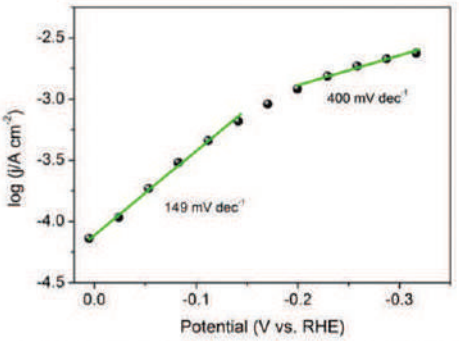

Fig. 7 Tafel (potential *vs.* log*j*) plot in CO_2-saturated 0.10 M phosphate buffer solution at pH 7.4. The current density (*j*) values were obtained from a linear sweep voltammetry experiment performed at 5 mV s^{-1}. The Tafel plot exhibited a slope of (149 ± 6) mV dec^{-1} from 0.005 V to −0.15 V and 400 mV dec^{-1} at larger overpotentials. The reported slopes are an average of 3 different measurements.

analysis (Fig. 7) evaluating the dependence of the electrocatalytic rate (log*J*) on the applied potential. The resulting Tafel plot is characterized by two different regimes, with a calculated slope of (149 ± 6) mV dec^{-1} at low overpotentials ($E < -0.2$ V), followed by a significant levelling off to a slope of (400 ± 16) mV dec^{-1}. These values are in perfect agreement with the electrocatalytic response expected for the Pd NPs as the competent hydrogenation sites.[21] In particular, the Tafel slope of (149 ± 6) mV dec^{-1}, which is consistent with a Pd-mediated hydride transfer mechanism, turns out to be the dominating regime also at higher *J* values, up to −0.2 V, with no mass transfer limitations.

Experimental section

Materials

Titanium butoxide (97%, $Ti(OBu)_4$), Nafion® 117 solution, mercapto-undecanoic acid (MUA) and tetrahydrofuran (THF) were purchased from Sigma-Aldrich. The single wall carbon nanohorns were obtained from Carbonium SRL, France. Absolute ethanol, anhydrous ultra-pure grade methanol and nitric acid (65%) were purchased from VWR Chemicals. Dibasic anhydrous sodium phosphate and monobasic sodium phosphate were purchased from Carlo Erba. $^{13}CO_2$ was purchased from Sigma-Aldrich and it contains 99% ^{13}C.

Synthesis of the oxidized SWCNHs

Pristine SWCNHs were dissolved in a 4 M nitric acid solution in order to obtain a suspension of 1 mg mL^{-1}. The suspension was sonicated for 15 minutes to dissolve the present bundles and then stirred for three hours. This optimized time is suitable to obtain the optimal degree of oxygenic groups and the lowest damage on the honeycomb structure surface.[48,49] The solid was then filtered and washed with distilled water until neutral pH of the washing water was reached (ox-SWCNHs).

Synthesis of the electrocatalysts

The electrocatalysts were synthesized by an adapted method previously described by Cargnello *et al.*[50] Briefly, an appropriate amount of MUA-protected Pd nanoparticles (Pd-MUAs) was dissolved in the required amount of titanium butoxide $Ti(OBu)_4$, in order to get the desired ratio components. The solution of the $Pd@TiO_2$ precursor was added dropwise to an ox-SWCNHs suspension (0.25 mg mL^{-1} in EtOH) under continuous sonication. The resulting suspension of "$Pd@Ti(OBu)_4$/ox-SWCNHs" was vigorously sonicated for 30 minutes. Finally, a mixture of H_2O (1.5 mL) and THF (13.5 mL) was added to ensure the complete hydrolysis of the Ti alkoxide. The mixture was sonicated for a further 30 min and then the product was filtered through a 0.45 μm PTFE filter, and washed with MeOH/H_2O 2 : 1 v/v and finally with MeOH. The final materials were dried at 80 °C overnight prior to being used ($Pd@TiO_2$/ox-SWCNHs). A similar approach was adopted in the absence of Pd-MUA in order to obtain the corresponding Pd-free catalyst (TiO_2/ox-SWCNHs).

For the synthesis of Pd/ox-SWCNHs, the ox-SWCNHs were sonicated in EtOH, and the appropriate amount of K_2PdCl_4 was added and the mixture was sonicated for 30 minutes. An aqueous solution of $NaBH_4$ was added and the mixture was sonicated for another 15 minutes. It was then filtered through a 0.45 μm PTFE filter and the solid was washed with water, followed by washing with EtOH, and dried at 80 °C overnight.

Characterization

The thermogravimetric analysis (TGA) of approximately 1 mg of each compound was performed on a TGA Q500 (TA Instruments) under either N_2 (N_2-TGA) or air (O_2-TGA), by equilibrating at 100 °C, and following a ramp of 10 °C min^{-1} up to 800 °C. Raman spectra were recorded using an Invia Renishaw microspectrometer (50) equipped with a He–Ne laser at 532 nm. To avoid sample damage or laser-induced heating/crystallization of the materials, the incident power was kept at 1% (full power of the laser is 100 mV). Powders were dispersed in EtOH, drop-cast onto a quartz slide and the solvent was evaporated; at least 5 spectra per sample were recorded on different areas of the sample in order to check the uniformity of the materials. Fourier Transform Infrared spectroscopy (FTIR) was performed using a System 2000 – Perkin Elmer spectrometer in the optical range of 370–4000 cm^{-1} at a resolution of 4 cm^{-1}. High resolution TEM (HRTEM) images were acquired using a JEOL 2200FS microscope operating at 200 kV, equipped with an Energy Dispersive Spectrometer (EDX), an in-column energy (Omega) filter, and a high-angle annular dark-field (HAADF) detector.

The textural properties have been analyzed by N_2 physisorption measurements at liquid nitrogen temperature using a Micromeritics ASAP 2020 analyzer. Prior to the analysis, the sample was degassed at 120 °C for 12 h. The surface area was calculated adopting the Brunauer–Emmett–Teller (BET) model while the pore size distribution was assessed following the Barrett–Joyner–Halenda (BJH) Analysis.

Metal accessibility has been checked by CO chemisorption at 35 °C using a Micromeritics ASAP 2020C analyzer. Prior to the analysis, the sample was reduced in H_2 at 120 °C for 1 h and then degassed at the same temperature for 12 h. A CO chemisorption isotherm was recorded in the 1–400 mmHg range with an equilibration time of at least 5 minutes for each point.

Reversible CO physisorption was subtracted by extrapolation of the linear range of the isotherm to zero. Metal surface area was calculated by assuming a chemisorption stoichiometry CO : Pd = 1 : 1.

^{13}C-NMR was performed on a 400 MHz Varian instrument. The samples were prepared by dissolving the electrolyte in D_2O and adding DMSO as an internal standard.

Electrochemical measurements. The electrochemical measurements were carried out at room temperature using an Autolab potentiostat/galvanostat (Model 302N) equipped with a three electrode cell under a stream of purified gasses that depending on the experiments were pure N_2 or CO_2. The working electrode was a 3 mm glassy carbon electrode (GCE; CH Instrument, CH 104), which prior to its surface modification with the nanohorn ink, was cleaned by polishing with 1.0 μm and 0.3 μm alumina slurries (micropolish Buehler) for 2 min and then washed with MilliQ water. A platinum wire was used as the counter electrode and an Ag/AgCl electrode (3 M, NaCl) (CH Instrument, CH 111) as the reference. All the reported potentials are converted to the RHE reference scale using E (*vs.* RHE) = E (*vs.* Ag/AgCl) + 0.210 V + 0.0591 V × pH whenever necessary. Bulk electrolysis experiments for product analysis were carried out using modified Toray carbon paper (Alfa Aesar, TGP-H-60) as the working electrode.

The nanohorn ink was prepared by dispersing 3 mg of the prepared ox-SWCNH, TiO_2/ox-SWCNH or Pd@TiO_2/ox-SWCNH powder in 1 mL of a (1 : 0.09 : 0.02) water:EtOH:nafion (2.5% in EtOH) solution. In each case, the slurry was subjected to ultrasonic agitation for 90 min until a homogeneous dispersion was obtained. Finally, 20 μL of the prepared ink was placed on the GCE surface and allowed to dry in an oven at 50 °C for 30 min. The catalytic electrodes obtained from diverse batch deposition and screened under identical conditions were found to display a performance variability of <10% in terms of current density, with analogous faraday efficiencies.

The cyclic voltammetry (CV) experiments were conducted in 0.1 M phosphate buffer solution, at pH 7.4 and at room temperature. Prior to each experiment, the electrolyte was saturated with N_2, Ar or CO_2 for 30 min. CV curves were recorded for the GCE coated with the ink layer in the potential range from 0.65 V to −0.85 V at a scan rate of 0.05 V s^{-1}. Current densities are reported normalizing the current by the electroactive area determined by chronoamperometry.

Bulk electrolysis experiments for product analysis were carried out using Toray carbon paper as the working electrode modified with 200 microliters of 3.0 mg mL^{-1} dispersion (corresponding to a Pd loading of 38 μg cm^{-2}). The modification was done by drop casting and the current densities are reported to be normalized by the geometric area covered by the drop.

TOF (H_2) calculation. The TOFs relative to the production of H_2 were calculated using the following formula:

$$\mathrm{TOF}(E) = \frac{Q(\mathrm{H_2}) - Q(\mathrm{background})}{Q(\mathrm{Pd}) \times \mathrm{time}} \times \mathrm{FE}$$

where TOF(E) is the TOF at an applied potential E, Q(H_2) is the total charge of the chronoamperometric experiment using the electrode with the modified material, Q(background) is the background current measured in the absence of the Pd nanoparticles, Q(Pd) is the charge associated with electroactive Pd, and FE is the faradaic efficiency.

Gas, ionic liquid chromatography and mass spectrometry. The products formed during the electrochemical reduction of CO_2 were analyzed by on-line gas chromatography (GC) and ionic chromatography (IC). For the gas phase analysis, the saturating gas (Ar or CO_2) was continuously bubbled through the electrolyte and analyzed on-line using an Agilent 7890 gas chromatograph equipped with a 10-way valve for injection and 2 analytical lines. CO possibly produced has been analyzed using a permanent gas/CO_2 column (parallel columns MolSieve 5A 10 m × 0.32 mm ID and PoraPlot Q 60 m × 0.53 mm ID) with He as the carrier gas and connected to a methanizer and a FID detector. H_2 was monitored using a MolSieve 5A (30 m × 0.53 mm) column using Ar as the carrier gas and connected to a TCD detector. The formate (HCO_2^-) formed in the liquid phase was quantified at the end of the electrolysis using a Metrohm 883 instrument equipped with a conductometric detector and a Metrosep A Supp5 250/4.0 column using a $NaHCO_3$ 1 mM/Na_2CO_3 3.2 mM solution as the mobile phase.

The qualitative analysis of the formed HCOOH was performed by SPME-GC/MS analysis. SPME extraction was performed with Supelco fibers coated with Carboxen/Polydimethylsiloxane (CAR/PDMS, thickness 75 μm). The method included inserting a new 1 cm CAR/PDMS fiber into a manual injection holder followed by preconditioning before the day's analyses. HCOOH was extracted by the static headspace method. During this step, the solution of 0.5 M $NaClO_4$ after the electrocatalytic reduction of CO_2 was transferred into a 10 mL vial, sealed with a screw cap and heated at 50 °C. Adsorption of HCOOH was performed by exposing the fiber for 10 min in the headspace of the vial. The adsorbed molecules were desorbed by introducing the SPME fiber into the injector of a 7890 Agilent gas chromatograph. The injector, in splitless mode for 2 min, was set at 270 °C. HCOOH was analysed using a DB-522 ms column (J&W, 60 m × 0.32 mm ID, 20 μm film), using He as the carrier gas. The mass spectra of the eluted HCOOH were acquired using a 5975C Agilent mass spectrometer, connected at the end of the GC column.

Faradaic efficiency (FE) calculation. The formic acid FE was calculated by the formula:

$$\mathrm{FE(HCOOH)} = \frac{Q_{\mathrm{HCOOH}}}{Q_{\mathrm{tot}}} \times 100$$

where Q_{HCOOH} is the charge associated with the formation of formic acid, calculated by the formula $Q_{\mathrm{HCOOH}} = nFe$, where n is the number of moles of formic acid formed during a chronoamperometric experiment (measured by ionic chromatography), F is the Faraday constant, and e = 2, that is the number of electrons involved in the reduction of CO_2 to formic acid. Q_{tot} is the total charge passed in the chronoamperometric experiment, calculated by the formula:

$$Q_{\mathrm{tot}} = \int_0^t I(t)\mathrm{d}t$$

(I = current, t = time of the experiment). For the calculation of FE(H_2), the method was the same but the charge was that associated with the formation of H_2 (Q_{H_2}). The moles of H_2 are measured by gas chromatography.

Conclusions

Hybrid heterostructures have been synthesized by integrating small Pd NPs (1.5 nm) within a TiO_2 environment powered by highly conductive SWCNH nano-scaffolds. The resulting nanomaterial provides a tunable platform for electrocatalytic H_2 storage/release technology, relying on CO_2 as a recyclable vector. In this perspective, the optimization of the interfacial synergy is of extreme interest as a function of the metal-hydride/metal-oxide "soft-hard" alternating phases and in combination with a tailored functionalization of the nanocarbon supports.

Conflicts of interest

There are no conflicts to declare.

Acknowledgements

The research leading to these results has received funding from the University of Trieste, INSTM, the Seventh Framework Programme [FP7/2007–2013] under grant agreement no. 310651 (SACS project). MVB acknowledges the support from the "ICTP TRIL Programme, Trieste, Italy". C. T. acknowledges the support from the Università degli Studi di Trieste, Finanziamento di Ateneo per progetti di ricerca scientifica, FRA2016.

Notes and references

1 M. Aresta, A. Dibenedetto and A. Angelini, *Chem. Rev.*, 2014, **114**, 1709–1742.
2 D. D. Zhu, J. L. Liu and S. Z. Qiao, *Adv. Mater.*, 2016, **28**, 3423–3452.
3 A. M. Appel, J. E. Bercaw, A. B. Bocarsly, H. Dobbek, D. L. DuBois, M. Dupuis, J. G. Ferry, E. Fujita, R. Hille, P. J. A. Kenis, C. A. Kerfeld, R. H. Morris, C. H. F. Peden, A. R. Portis, S. W. Ragsdale, T. B. Rauchfuss, J. N. H. Reek, L. C. Seefeldt, R. K. Thauer and G. L. Waldrop, *Chem. Rev.*, 2013, **113**, 6621–6658.
4 F. A. Armstrong and J. Hirst, *Proc. Natl. Acad. Sci. U. S. A.*, 2011, **108**, 14049–14054.
5 A. Bassegoda, C. Madden, D. W. Wakerley, E. Reisner and J. Hirst, *J. Am. Chem. Soc.*, 2014, **136**, 15473–15476.
6 J. A. Turner, *Science*, 2004, **305**, 972–974.
7 K. C. Christoforidis and P. Fornasiero, *ChemCatChem*, 2017, **9**, 1523–1544.
8 A. Álvarez, A. Bansode, A. Urakawa, A. V. Bavykina, T. A. Wezendonk, M. Makkee, J. Gascon and F. Kapteijn, *Chem. Rev.*, 2017, **117**, 9804–9838.
9 E. J. Popczun, C. G. Read, C. W. Roske, N. S. Lewis and R. E. Schaak, *Angew. Chem., Int. Ed.*, 2014, **53**, 5427–5430.
10 B. Cao, G. M. Veith, J. C. Neuefeind, R. R. Adzic and P. G. Khalifah, *J. Am. Chem. Soc.*, 2013, **135**, 19186–19192.
11 J. Kibsgaard, T. F. Jaramillo and F. Besenbacher, *Nat. Chem.*, 2014, **6**, 248–253.
12 Y. Li, H. Wang, L. Xie, Y. Liang, G. Hong and H. Dai, *J. Am. Chem. Soc.*, 2011, **133**, 7296–7299.
13 M. Tagliapietra, A. Squarcina, N. Hickey, R. De Zorzi, S. Geremia, A. Sartorel and M. Bonchio, *ChemSusChem*, 2017, **10**, 4430–4435.
14 J. Ying, G. Jiang, Z. Paul Cano, L. Han, X.-Y. Yang and Z. Chen, *Nano Energy*, 2017, **40**, 88–94.
15 R. Mazzaro, A. Boni, G. Valenti, M. Marcaccio, F. Paolucci, L. Ortolani, V. Morandi, P. Ceroni and G. Bergamini, *ChemistryOpen*, 2015, **4**, 268–273.
16 F.-Q. Shao, X.-Y. Zhu, A.-J. Wang, K.-M. Fang, J. Yuan and J.-J. Feng, *J. Colloid Interface Sci.*, 2017, **505**, 307–314.
17 B. C. Marepally, C. Ampelli, C. Genovese, T. Saboo, S. Perathoner, F. M. Wisser, L. Veyre, J. Canivet, E. A. Quadrelli and G. Centi, *ChemSusChem*, 2017, **10**, 4442–4446.
18 M. Ma, H. A. Hansen, M. Valenti, Z. Wang, A. Cao, M. Dong and W. A. Smith, *Nano Energy*, 2017, **42**, 51–57.
19 E. S. Gutterød, S. Øien-Ødegaard, K. Bossers, A.-E. Nieuwelink, M. Manzoli, L. Braglia, A. Lazzarini, E. Borfecchia, S. Ahmadigoltapeh, B. Bouchevreau, B. T. Lønstad-Bleken, R. Henry, C. Lamberti, S. Bordiga, B. M. Weckhuysen, K. P. Lillerud and U. Olsbye, *Chem. Ind. Eng. Prog.*, 2017, **56**, 13206–13218.
20 K. S. Egorova and V. P. Ananikov, *Angew. Chem., Int. Ed.*, 2016, **55**, 12150–12162.
21 X. Min and M. W. Kanan, *J. Am. Chem. Soc.*, 2015, **137**, 4701–4708.
22 C. J. Stalder, S. Chao and M. S. Wrighton, *J. Am. Chem. Soc.*, 1984, **106**, 3673–3675.
23 R. Kortlever, C. Balemans, Y. Kwon and M. T. M. Koper, *Catal. Today*, 2015, **244**, 58–62.
24 G. Valenti, A. Boni, M. Melchionna, M. Cargnello, L. Nasi, G. Bertoni, R. J. Gorte, M. Marcaccio, S. Rapino, M. Bonchio, P. Fornasiero, M. Prato and F. Paolucci, *Nat. Commun.*, 2016, **7**, 13549.
25 S. Akbayrak, Y. Tonbul and S. Özkar, *Appl. Catal., B*, 2017, **206**, 384–392.
26 A. Beltram, M. Melchionna, T. Montini, L. Nasi, P. Fornasiero and M. Prato, *Green Chem.*, 2017, **19**, 2379–2389.
27 M. Cargnello, J. J. D. Jaén, J. C. H. Garrido, K. Bakhmutsky, T. Montini, J. J. C. Gámez, R. J. Gorte and P. Fornasiero, *Science*, 2012, **337**, 713–717.
28 K. Bakhmutsky, N. L. Wieder, M. Cargnello, B. Galloway, P. Fornasiero and R. J. Gorte, *ChemSusChem*, 2012, **5**, 140–148.
29 M. Melchionna, A. Beltram, T. Montini, M. Monai, L. Nasi, P. Fornasiero and M. Prato, *Chem. Commun.*, 2016, **52**, 764–767.
30 L. Robert, H. Anming, P. John and Y. N. Zhou, *Nano-Micro Lett.*, 2013, **5**, 202–212.

31 J. Shen, B. Yan, M. Shi, H. Ma, N. Li and M. Ye, *J. Mater. Chem.*, 2011, **21**, 3415–3421.

32 G. Lu, H. Wang, Z. Y. Bian and X. Liu, *Sci. World J.*, 2013, 424617.

33 S. Berber, Y. K. Kwon and D. Tomanek, *Phys. Rev. B: Condens. Matter Mater. Phys.*, 2000, **62**, R2291–R2294.

34 G. Pagona, N. Tagmatarchis, J. Fan, M. Yudasaka and S. Iijima, *Chem. Mater.*, 2006, **18**, 3918–3920.

35 E. Bekyarova, K. Murata, M. Yudasaka, D. Kasuya, S. Iijima, H. Tanaka, H. Kahoh and K. Kaneko, *J. Phys. Chem. B*, 2003, **107**, 4681–4684.

36 K. Urita, S. Seki, S. Utsumi, D. Noguchi, H. Kanoh, H. Tanaka, Y. Hattori, Y. Ochiai, N. Aoki, M. Yudasaka, S. Iijima and K. Kaneko, *Nano Lett.*, 2006, **6**, 1325–1328.

37 M. Cargnello, N. L. Wieder, P. Canton, T. Montini, G. Giambastiani, A. Benedetti, R. J. Gorte and P. Fornasiero, *Chem. Mater.*, 2011, **23**, 3961–3969.

38 A. Hashimoto, H. Yorimitsu, K. Ajima, K. Suenaga, H. Isobe, A. Miyawaki, M. Yudasaka, S. Iijima and E. Nakamura, *Proc. Natl. Acad. Sci. U. S. A.*, 2004, **101**, 8527–8530.

39 V. Krungleviciute, C. A. Ziegler, S. R. Banjara, M. Yudasaka, S. Iijima and A. D. Migone, *Langmuir*, 2013, **29**, 9388–9397.

40 M. S. Dresselhaus, A. Jorio, M. Hofmann, G. Dresselhaus and R. Saito, *Nano Lett.*, 2010, **10**, 751–758.

41 O. Frank, M. Zukalova, B. Laskova, J. Kurti, J. Koltai and L. Kavan, *Phys. Chem. Chem. Phys.*, 2012, **14**, 14567–14572.

42 U. J. Kim, C. A. Furtado, X. M. Liu, G. G. Chen and P. C. Eklund, *J. Am. Chem. Soc.*, 2005, **127**, 15437–15445.

43 G. K. Ramesha, J. F. Brennecke and P. V. Kamat, *ACS Catal.*, 2014, **4**, 3249–3254.

44 M. Grden, M. Lukaszewski, G. Jerkiewicz and A. Czerwinski, *Electrochim. Acta*, 2008, **53**, 7583–7598.

45 K. Cheng, D. X. Cao, F. Yang, L. L. Zhang, Y. Xu and G. L. Wang, *J. Mater. Chem.*, 2012, **22**, 850–855.

46 Z. P. Li, X. C. Yang, N. Tsumori, Z. Liu, Y. Himeda, T. Autrey and Q. Xua, *ACS Catal.*, 2017, **7**, 2720–2724.

47 Q.-L. Zhu, N. Tsumori and Q. Xu, *J. Am. Chem. Soc.*, 2015, **137**, 11743–11748.

48 B. Niu, W. Xu, Z. D. Guo, N. Z. Zhou, Y. Liu, Z. J. Shi and Y. F. Lian, *J. Nanosci. Nanotechnol.*, 2012, **12**, 7376–7381.

49 I. Gerber, M. Oubenali, R. Bacsa, J. Durand, A. Goncalves, M. F. R. Pereira, F. Jolibois, L. Perrin, R. Poteau and P. Serp, *Chem. – Eur J*, 2011, **17**, 11467–11477.

50 M. Cargnello, M. Grzelczak, B. Rodríguez-Gonzáález, Z. Syrgiannis, K. Bakhmutsky, V. La Parola, L. M. Liz-Marzán, R. J. Gorte, M. Prato and P. Fornasiero, *J. Am. Chem. Soc.*, 2012, **134**, 11760–11766.